



PCCP

Structural analysis of initial lithiation of NiO thin film electrodes

| | |
|-------------------------------|---|
| Journal: | <i>Physical Chemistry Chemical Physics</i> |
| Manuscript ID | CP-ART-03-2019-001527.R1 |
| Article Type: | Paper |
| Date Submitted by the Author: | 03-Apr-2019 |
| Complete List of Authors: | Evmenenko, Guennadi; Northwestern University, Fister, Tim; Argonne National Laboratory, Chemical Sciences and Engineering Castro, Fernando; Northwestern University, Materials Science and Engineering Chen, Xinqi; Northwestern University, Lee, Byeongdu; Argonne National Laboratory, X-ray Sciences Division; Buchholz, Donald; Northwestern University, Materials Research Institute Dravid, Vinayak; Northwestern University, Materials Science & Engineering Fenter, Paul; Argonne National Laboratory Bedzyk, Michael; Northwestern University, Materials Science and Engineering |
| | |

SCHOLARONE™
Manuscripts

Structural analysis of initial lithiation of NiO thin film electrodes

Guennadi Evmenenko,^a Timothy T. Fister,^b Fernando C. Castro,^a Xinqi Chen,^{c,d} Byeongdu Lee,^e
D. Bruce Buchholz,^a Vinayak P. Dravid,^a Paul Fenter,^b Michael J. Bedzyk^{a,f,*}

^a *Department of Materials Science and Engineering, Northwestern University, Evanston, Illinois 60208, USA*

^b *Chemical Sciences and Engineering Division, Argonne National Laboratory, Lemont, Illinois 60439, USA*

^c *NUANCE Center, Northwestern University, Evanston, Illinois 60208, USA*

^d *Department of Mechanical Engineering, Northwestern University, Evanston, Illinois 60208, USA*

^e *X-ray Science Division, Argonne National Laboratory, Lemont, Illinois 60439, USA*

^f *Department of Physics and Astronomy, Northwestern University, Evanston, Illinois 60208, USA*

* Corresponding author: bedzyk@northwestern.edu

Abstract

Observations of the initial lithiation of NiO electrodes demonstrate how to seed the conversion reactions using interfaces in a thin film Ni/NiO bilayer architecture. Operando X-ray reflectivity (XRR) reveals that structural changes in a NiO film begin at potentials near the theoretical reduction potential (1.8-2.0 V) with detectable lithiation of both the buried Ni/NiO interface and the outer NiO surface that occur prior to the reaction of the NiO film. This initial conversion reaction is most pronounced in ultrathin NiO films (~20 Å) with only small changes to the NiO film surface for thicker films (~67 Å). The limited reactivity of thicker NiO films probed using *operando* grazing incidence small-angle X-ray scattering (GISAXS) shows the growth of nanoparticles at the electrode / electrolyte interface during initial lithium ion insertion, with a 16-20 Å average radius. *Ex-situ* X-ray photoelectron spectroscopy (XPS), time-of-flight secondary ion mass spectrometry (ToF-SIMS), and scanning transmission electron microscopy / electron energy loss spectroscopy (STEM/EELS) confirm our conclusions about the morphological changes accompanying initial stage of lithiation in these conversion reaction electrodes. The present study reveals the interconnected challenges of solid-solid transitions, overpotentials, interfacial nucleation and kinetics, and transition metal dissolution in conversion-type electrodes that are critical for their use as electrodes in lithium-ion batteries.

KEYWORDS: *thin-film electrode, nickel oxide, conversion reactions, overpotential, lithium-ion battery*

Introduction

With progress of knowledge of electrode materials, it has been found that their surface structures are of great importance to the electrochemical performance of Li-ion batteries. The interfaces between the electrolyte and the two electrodes dictate the performance of the devices. Understanding reactions at the solid electrolyte interphase (SEI) is essential to developing strategies to enhance cycle life and safety of Li-ion batteries. Despite considerable research in the past few decades,¹⁻⁵ much remains to be understood at the fundamental level. A powerful approach to understand interfacial phenomena in Li-ion batteries is the use of thin-film samples of the active materials as model systems. Especially this strategy is feasible for metal oxide electrodes that undergo so-called conversion reactions, eventually fragmenting the original structure into nanoparticles of lithia and metal.⁶

The specific capacity of traditional lithium ion battery (LIB) cathodes is limited by the available Li-site density for intercalation.^{7,8} Conversion materials offer the possibility of much higher specific capacities ($> 500 \text{ mA h g}^{-1}$) that scale with the number density of the reacting anion species.⁹⁻¹¹ In the case of oxides, this process is associated with the complete reduction of a metal oxide into a composite electrode consisting of nano-sized metallic and Li_2O particles.⁶ However, the use of conversion materials is limited by multiple issues related to large solid-solid phase transitions, electronic and ionic impedance, overpotentials (the potential difference between a thermodynamically determined voltage and the actual insertion voltage under operating conditions), internal polarization, interfacial nucleation, and by a substantial electrolyte involvement in the electrochemical process.⁹ In particular, the resulting voltage hysteresis between charge and discharge voltage has essentially precluded oxide conversion materials from any practical application.⁹

Overcoming these significant obstacles is necessary for the adoption of conversion materials into commercial devices and requires a full understanding of the relevant reaction mechanisms. Substantial overpotentials observed for conversion reactions are associated with the nucleation of metal nanoparticles within a Li_2O matrix.¹⁰⁻¹¹ From the perspective of classical nucleation theory,¹² this is controlled by the interfacial energy associated with the metal- Li_2O interface, leading to overpotentials in the experimental conversion potentials with respect to the theoretical values.^{10,13,14} Theoretically predicted potentials are calculated based on equilibrium electrochemical thermodynamics from the relation between free energy and the maximum electrical work that can be performed, expressed in terms of the electrode potential E of a half-cell.¹⁵ Potential values at which conversion reactions have

experimentally been observed to occur for different compounds during the first discharge in a lithium battery and deviation from the thermodynamic value calculated for the bulk are listed in Ref. 10. Additionally, nonequilibrium reaction paths can contribute significantly to the conversion mechanism of transition metal oxide electrodes during lithiation.¹⁶ Recently, it was found that in addition to bulk, three-dimensional conversion occurring at previously measured potentials, lithiation can occur with little or no overpotential at the buried Ni/NiO interface.¹⁷ This new phenomenon is preceded by an accumulation of lithium at the buried metal/oxide interfaces at even higher potentials.

Despite these new insights, conversion reactions at the electrode/electrolyte surface and their role in the formation of solid electrolyte interphase (SEI) compounds remain largely unexplored. Previous studies showed that thin films provide similar benefits to nanophased oxides for conversion reactions, with better-defined interfaces that can nucleate and confine the reaction products.^{6,18-33} Here we extend previous analysis of vertical changes in the structure of Ni/NiO bilayers^{34,35} with *operando* grazing incidence small angle X-ray scattering (GISAXS) to analyze particle formation at the electrode/electrolyte interface. NiO was chosen as a model system due the simplicity of its displacement reaction: $\text{NiO} + 2\text{Li}^+ + 2\text{e}^- \leftrightarrow \text{Ni} + \text{Li}_2\text{O}$ and its substantial overpotential that separates bulk and interfacial reactivity ($E_{eq} = 1.8 \text{ V}$; $E_{exp} = 0.6 \text{ V}$). The composition of the SEI after lithiation was studied further using X-ray photoelectron spectroscopy (XPS), time-of-flight secondary ion mass spectrometry (ToF-SIMS) depth profiling, and scanning transmission electron microscopy / electron energy loss spectroscopy (STEM/EELS). The results reveal that conversion reactions and structural changes in NiO thin film electrodes begin at potentials near the equilibrium lithiation potential. These changes are characterized by the formation of low electron density region close to the buffer Ni layer; conversion reaction of the NiO film surface and the nucleation of reduced Ni in the form of $R_g \sim 16\text{-}20 \text{ \AA}$ nanoparticles in the SEI.

Experimental

The amorphous nickel metal / nickel oxide multilayer films were grown at room temperature by pulsed-laser deposition (PLD) on $10 \times 3 \times 1 \text{ mm}^3$ sapphire $\alpha\text{-Al}_2\text{O}_3$ (1-102) substrates (CrysTec GmbH, Germany). PLD was accomplished a PVD Products PLD/MBE 2300 which employed a 248 nm KrF excimer laser with a 25 ns pulse duration and operated at 2 Hz. The laser pulse was focused onto a 1.5 mm x 2.5 mm spot size. Separate targets were used to grow Ni/NiO bilayers with the thickness of each layer controlled by adjusting the number of laser pulses. The targets were rotated at 5-rpm about their axis to prevent localized heating. The target-substrate separation was fixed at 10 cm. Nickel was deposited at room

temperature from a metallic nickel target at an energy of 300 mJ per pulse at the chamber base pressure, $\sim 5 \times 10^{-7}$ Torr, without the introduction of a reactant gas. After the deposition of the nickel layer, the substrates were removed from the chamber to mask the outer edges of the substrate with Kapton® tape to prevent nickel oxide from being deposited on the *in operando* contact areas. The substrates were then returned to the deposition chamber and pumped back to the base pressure. Nickel oxide was deposited at room temperature over the nickel in the center 4 mm of the substrate from a dense hot-pressed nickel oxide target at an energy of 200 mJ per pulse in a deposition ambient of 5×10^{-4} Torr UHP oxygen. This set of deposition parameters has been established to form a nickel oxide film.^{36,37}

The pristine films were first characterized with *ex situ* X-ray reflectivity measurements, using a Rigaku ATXG diffractometer (X-ray Diffraction Facility, NU) with $E = 8.041$ keV ($\lambda = 1.542$ Å) X-rays and 0.1 (v) \times 2.0 (h) mm² beam size. This gives the ability to control and optimize the structural parameters of the PLD-grown films and to increase our effectiveness of in-operando measurements using the limited synchrotron beamtime.

The *in situ* XRR experiments were performed at the Advanced Photon Source (APS) 33BM station at a photon energy of $E = 20.00$ keV.³⁸ The X-ray beam size was collimated to 1.0×0.25 mm² and the scattered X-ray intensity was acquired with a Pilatus 100k detector. 15-minute duration reflectivity scans were measured repeatedly during the 9 h first discharge of the electrochemical cycle of the as-deposited film starting at the open circuit condition to 0.3 V. The samples were contained in an X-ray compatible electrochemical cell with a lithium metal counter and reference electrodes³⁹ and fully immersed in a 1 M solution of LiClO₄ or LiPF₆ in 1:1 ratio of ethylene carbonate and dimethyl carbonate by volume; hence, all reported potentials are relative to the Li/Li⁺ redox couple. The as-deposited samples had an open circuit (OC) potential of 3.2-3.3 V when initially placed in the electrochemical cell. XRR analysis used Motofit with a multiple-slab model that included a sapphire substrate, Ni/NiO layers, and an electrolyte.⁴⁰ Structural parameters for sapphire and the electrolyte were fixed, whereas the parameters for the buffer and active layers (electron density, interface roughness, and layer thickness) were allowed to vary. The electron densities were initially estimated based on the chemical composition of the electrode components. Table S1 lists calculated electron densities of bulk materials relevant to this study. For lithiated samples the structural model included variable electron densities and thicknesses of active NiO-based layers and variable Ni-layer thicknesses with an electron density that was fixed to a value obtained from the analysis of the pristine as-deposited samples. In some cases, the fits made use of a parameter that nominally varies the energy resolution of the X-ray beam. In this case, this parameter is used as a

phenomenological approach to incorporate the lateral heterogeneity of the multilayer structure (e.g., the layer spacing).

Operando GISAXS experiments were conducted at the 12ID-B station at the Advanced Photon Source (APS) at Argonne National Laboratory. The samples were probed using 14.00 keV ($\lambda = 0.8856$ Å) X-rays of 16 (v) \times 100 (h) μm^2 beam size at a sample-to-detector distance of approximately 1.9-2.0 m, calibrated using a silver behenate standard. Scattered radiation was recorded using a Pilatus2M area detector. The angles of incidence were chosen to be $\alpha = 0.12^\circ$ - 0.20° , in the vicinity of the 0.19° critical angle for the NiO film immersed in electrolyte. The data reduction (i.e. correcting the 2D data and converting the data from the angle of the detector pixel into reciprocal space - $q = \frac{4\pi}{\lambda} \sin \theta$ is the magnitude of the scattering wave vector, 2θ is the scattering angle) was performed by GISAXSshop.⁴¹ GISAXS data analysis used the IRENA software package.⁴²

XPS analysis was carried out using a Thermo Scientific ESCALAB 250 Xi equipped with a monochromatic 300 W Al anode X-ray source (1486.6 eV). The X-ray spot size was 500 μm in diameter. High-resolution scans used a pass energy of 50 eV, a 50 ms dwell time, and a 0.1 eV step size. Depth profiling used a 3000 eV Ar ion beam sputtered over an area of 2000 μm^2 . The sputtering condition was 3000 eV and 17 μA current. An electron flood gun and ion beam were applied to the sample surface to neutralize surface charging effects. All XPS spectra were calibrated in binding energy with Ni^0 at 852.4 eV.⁴³

Elemental depth profiling was also carried out with time of flight secondary ion mass spectrometer (ToF-SIMS, PHI TRIFT III). A 5 kV unbunched Ga^+ ion beam was used to sputter a 200 μm^2 crater on a flat surface of the sample, and a 5 kV bunched Ga^+ ion beam was used for analysis in the central 25 μm^2 area. Each cycle included 30 seconds analysis, 60 seconds sputtering, and 2 seconds charge compensation. The mass peaks of Al ($m/z = 27$), AlO ($m/z = 43$), AlH ($m/z = 28$), Li ($m/z = 7$), and Ni ($m/z = 58$) were selected for depth profiling. The extracted current and ion dose was kept constant during the whole experiment. The sputter crater was measured with a stylus profilometer (Veeco Dektak 150) and then used to calculate the sputtering rate.

After first cycle discharging of the sample from the open circuit potential for the as-deposited sample to potential of 1.7 V, each Ni/NiO thin film sample was analyzed by ToF-SIMS. As a control sample, we used the pristine sample from the same PLD batch that was spin-coated by PMMA (polymethyl methacrylate) with a molecular weight of 495,000 (M_w). A Laurell WS-400-6NPP-LITE spin coater was used to deposit resin film from 3 wt % solution of PMMA in anisole (spin speed of 4000 rpm for 30 seconds). The sample was dried overnight in a vacuum oven at 60°C before the ToF-SIMS experiment.

After first cycle discharging the as-deposited sample from the open circuit potential (3.3 V) to a potential of 1.7 V, select multilayer samples were also examined using transmission electron microscopy (TEM), STEM, and EELS. Cross-sections of the bilayer films were prepared using a FEI Helios Nanolab 600 Dual Beam focused ion beam (FIB) system in order to view changes to the structure and composition within each distinct layer. TEM, STEM, and EELS analysis were all done using a JEOL 2100F TEM/STEM with a 200 kV operating voltage. EELS measurements were acquired with a convergence semi-angle of 8.4 mrad and collection semi-angle of 14 mrad. To determine the Ni L₃/L₂ intensity ratio, the EELS signal was integrated over energy windows of 850 eV – 865 eV and 870 eV – 880 eV for the Ni L₃ and L₂ edges, respectively.

Results and Discussion

We started the investigation of structural changes in bilayer Ni/NiO electrodes with *operando* XRR measurements to examine behavior during the first discharge (i.e. lithiation) reaction. Two sets of bilayer films were initially used: ~49 Å-thick Ni/67 Å NiO and ~49 Å-thick Ni/19 Å NiO. The lithiation of these layers was performed under potentiostatic control starting with the as-deposited film at the open circuit condition (3.2-3.3 V). X-ray reflectivity patterns were measured repeatedly during cyclic voltammetry (CV) scans between the open circuit potential of the pristine structure and 0.3 V (with respect to Li/Li⁺), with the sweep rate of 0.1 mV s⁻¹. The first discharge voltammograms taken during these measurements are shown in Figure S1. An abrupt onset of lithiation for 67 Å-thick NiO film occurs near 0.7 V corresponding to the previously observed phase transition of NiO to metallic Ni,^{34,35} whereas the reduction peak for 19 Å-thick NiO film is broader and asymmetrically shaped starting near 0.9 V and going to its minimum at 0.5 V.

Fig. 1 shows specular X-ray reflectivity patterns and the corresponding electron density profiles for the film with 67 Å NiO layer. As seen from Fig. 1B, only subtle changes to the NiO electron density are observed near the theoretically predicted lithiation potential of 1.8 V as compared with the pristine sample. The only changes that are observed include a slight reduction in the density at the Ni/NiO interface (presumably as a result of lithium build up and possible initial interfacial nucleation of the nickel in the oxide layer)¹⁷ and the smearing of NiO/electrolyte interface due to reactions at the surface of the NiO film. Apart from these interfacial changes, the electron density of the NiO film and its thickness are nearly equal to the pristine film. An abrupt onset for lithiation occurs near 0.7 V (consistent with the CV data, Fig. S1, and more than 1 V lower than the theoretical lithiation potential), when the

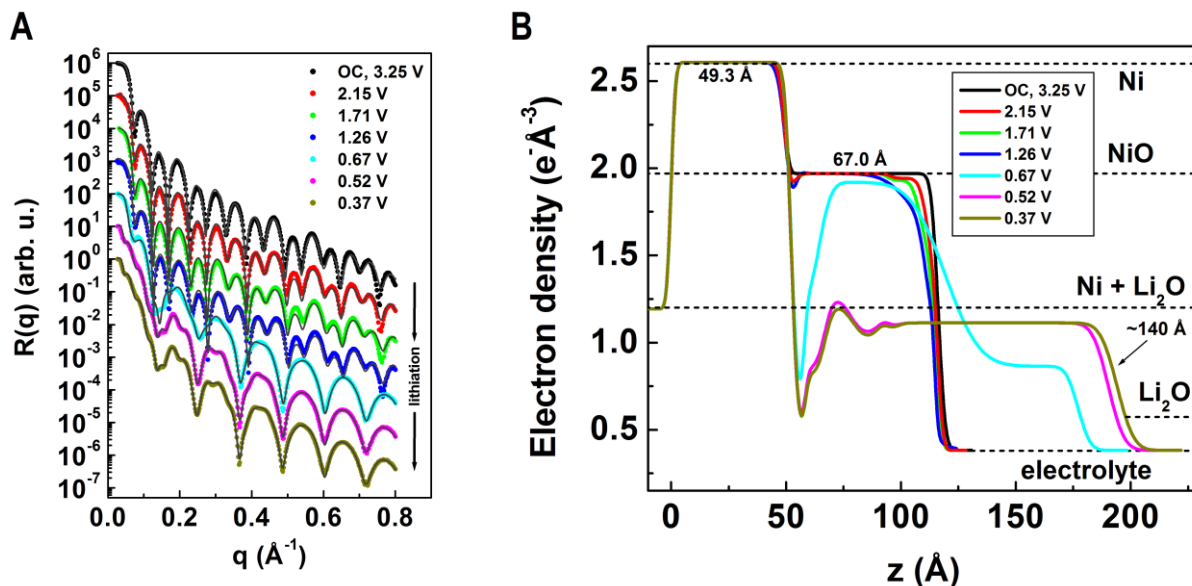


Fig. 1 (A) Operando specular XRR data (solid circles) and best fits (solid lines) for the Ni (49.3 Å) / NiO (67.0 Å) bilayer film during the first discharge (lithiation). (B) Electron density profiles obtained from best fits of the XRR data shown in (A). Calculated electron densities for the electrolyte, Ni, NiO, Li₂O and expected electron density of the fully lithiated NiO layer (Ni + Li₂O) are shown by dotted lines for comparison.

electron density of the oxide layer drops to a value nearly equivalent to the calculated value of $1.20 \text{ e}^- \text{Å}^{-3}$, corresponding to the stoichiometric mixture of Ni and Li₂O associated with fully lithiated NiO. The density changes are accompanied by a two-fold expansion of the active layer thickness. Stronger density modulations near the surface of the nickel current collector reflect a vertical stratification of the Li₂O and Ni components. Similar morphological changes of active layers during lithiation were observed in our earlier studies using multilayer Ni/NiO electrodes.³⁵

This behavior is in contrast to a thinner 19 Å-thick NiO film, which exhibits significant morphological changes that begin at high potentials (starting at 2.52 V, even above the theoretical bulk lithiation potential) (Fig. 2). These results show that this reaction is associated with significant changes to the NiO film electron density. Moreover, these structural changes evolve gradually as the potential decreases to ~ 0.7 V, where it develops a uniform electron density profile having a value equivalent to the fully lithiated, two-fold expanded NiO layer. This XRR analysis confirms our previous finding that a lithium space charge layer is a crucial component for the conversion of NiO, observed here as a reduction of the electron density at the Ni/NiO interface at 2.52 V. This was previously found to be a key component for reducing energy barriers in a potential-dependent nucleation model for conversion based on density functional theory.¹⁷ The comparison of the results of Figs 1 and 2 reveals that this behavior is mostly expressed for ultrathin films, while larger film thickness slows propagation of the conversion reaction

through the film.

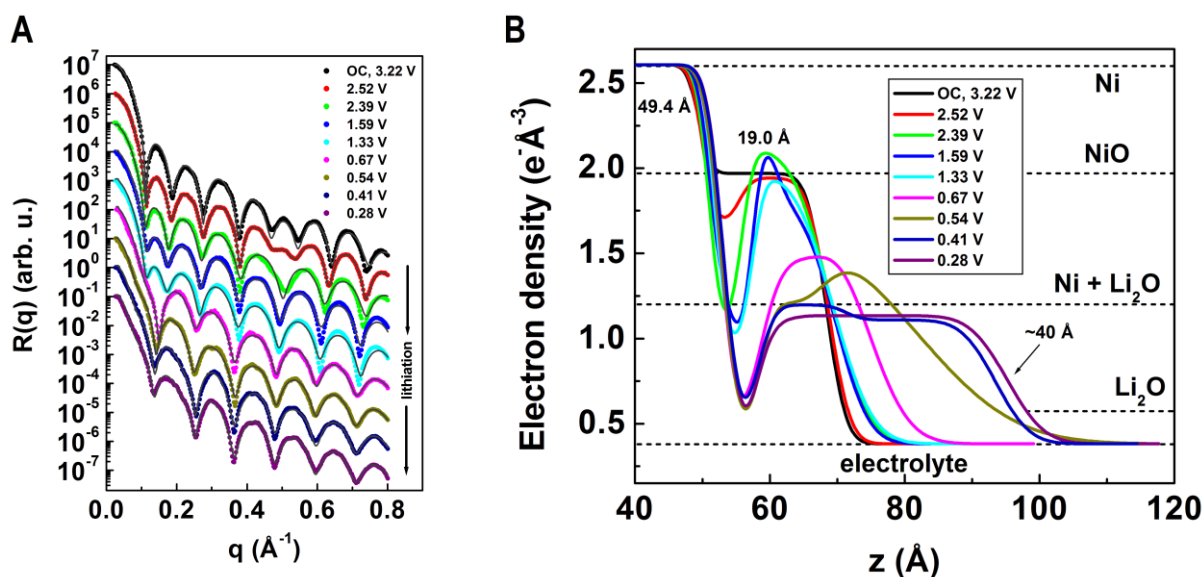


Fig. 2 (A) Operando specular XRR data (solid circles) and best fits (solid lines) for the Ni (49.4 \text{\AA}) / NiO (19.0 \text{\AA}) bilayer electrodes during the first discharge (lithiation). (B) Electron density profiles obtained from best fits of the XRR data shown in (A). Calculated electron densities for the electrolyte, Ni, NiO, Li₂O and expected electron density of the fully lithiated NiO layer (Ni + Li₂O) are shown by dotted lines for comparison.

As seen from XRR measurements, there is an accumulation of lithium at the buried metal/oxide interfaces in the bilayer structure and the initial lithiation process of thin Ni/NiO films starts at potentials higher than either the experimentally observed values of 0.6-0.7 V for bulk and thick film electrodes or even the theoretical bulk lithiation potential. Another morphological change that was observed at high potentials is the smearing of the top NiO/electrolyte interface. These changes likely only hint at the range of processes occurring at the surface. For instance, the formation of SEI components is also largely hidden from XRR studies due the similar density of decomposition phases with the electrolyte and their non-uniform surface coverage. To better understand processes occurring at the surface, we applied additional techniques to clarify the structural changes and morphological evolution of conversion thin film electrodes at potentials above 1 V.

To highlight products forming at and above the surface, we applied advanced grazing-incidence techniques that can reveal the structures of materials near the surface.⁴⁴ While 2D electrodes (i.e. thin films) scatter almost entirely vertically (along q_z), three-dimensional nucleation of conversion products or SEI species give rise to additional in-plane GISAXS intensity (at nonzero q_{xy}). Moreover, it is possible to alter the depth sensitivity of the measurement by changing the incident angle (α), which affects the X-ray penetration depth. Here, *operando* GISAXS was used to study the growth of reduced Ni nanoparticles

in NiO films during initial lithiation as a function of film thicknesses. For GISAXS measurements, we used the same X-ray compatible cell from the XRR studies, starting at the open circuit condition of the as-deposited NiO films, similar to XRR experiments described above. GISAXS images were then collected repeatedly during CV scans between the open circuit potential of the pristine structure and 0.3 V with the sweep rate of 0.1 mV s^{-1} for the two bilayer Ni/NiO film samples, with NiO thicknesses of 67 \AA and 19 \AA . The first discharge voltammograms taken during these measurements are shown in Fig. S2. These are similar to voltammograms previously observed during *operando* XRR measurements (Fig. S1). Fig. 3 shows 2D GISAXS patterns for Ni/NiO films recorded during the first discharge. Just from changes to the raw GISAXS patterns, it is clear that scattering for 19 \AA -thick NiO starts to increase in the potential range of 2.50 to 2.06 V, whereas for thicker 67 \AA film these changes begin in a lower voltage range, from 2.17 to 1.54 V. In both cases, there is an increase in scattering intensity at potentials close to the theoretically predicted lithiation potential. This intensity increase is correlated to laterally

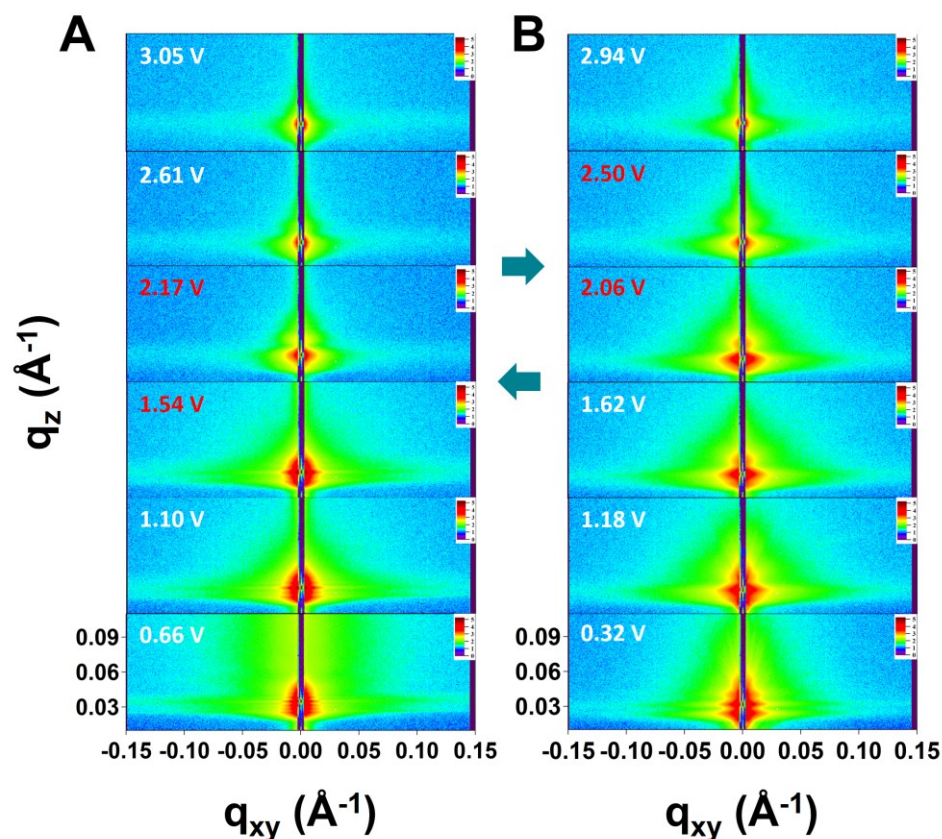


Fig. 3. Operando GISAXS patterns for Ni (49.3 \AA) / NiO (67.0 \AA) (A) and Ni (49.4 \AA) / NiO (19.0 \AA) (B) bilayer electrodes during lithiation ($\alpha = 0.135^\circ$). Teal block arrows show where an increase in scattering intensity begins.

heterogeneous changes to the electron density, such as nanoscopic objects, in the NiO film immersed in = $\alpha + \alpha_c$ relative to the direct beam on the detector, where α and α_c are incident and critical angles for electrolyte. Horizontal linecuts of the 2D GISAXS patterns were taken at the Yoneda peak positions α_Y the GISAXS experiment.^{44,45} The overall size of scattering entities can be estimated from the SAXS radius of gyration, R_g .⁴⁶ To determine R_g , we applied the Guinier approximation to the horizontal linecuts: $I(q) = I(0) \exp(-qR_g^2/3)$, where $I(0)$ is the scattering intensity at zero angle ($q = 0$).⁴⁷ The Guinier representation of the scattered intensity in the low q -regime as a function of potential is shown for both Ni/NiO films in Fig. 4. Distinct increases in the scattering intensity occur near the theoretical lithiation potential. The linear character of $\ln(I)$ vs q^2 indicates a low concentration of scatterers in the system. Fits

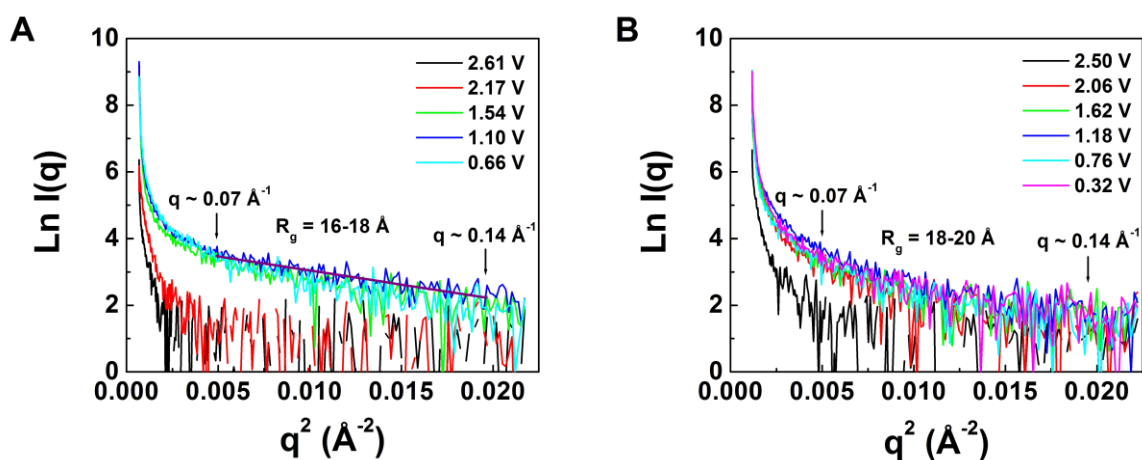


Fig. 4. Guinier plots of horizontal line cuts derived from the 2D GISAXS patterns shown in Figure 3: (A) Ni (49.3 Å) / NiO (67.0 Å) and (B) Ni (49.4 Å) / NiO (19.0 Å) bilayer electrodes. The limits for the q -range to determine R_g are indicated by arrows. Linear fit of the experimental curve for 1.10 V is shown on the plot of Fig. 4A by purple solid line as an example.

to the GISAXS data show that nanoparticles with $R_g \sim 16\text{-}20$ Å are formed during the initial stage of NiO lithiation at high potentials, and the size of these entities does not change significantly as the conversion reaction proceeds at lower potentials.

In the GISAXS experiment, the penetration depth of X-rays into the NiO film immersed in electrolyte can be varied as a function of incident angle α (Fig. S3). Fig. S4 shows Guinier plots of horizontal linecuts of 2D GISAXS patterns at different incident angles for the bilayer Ni (50 Å) / NiO (200 Å) electrode during lithiation. An incident angle of $\alpha = 0.12^\circ$ gives a penetration depth of ~ 27 Å that corresponds to surface penetration of X-rays, whereas at $\alpha = 0.20^\circ$ the penetration depth is ~ 240 Å and X-rays penetrate entirely through the Ni/NiO film. Because these GISAXS results are similar for the shallow and deeper penetration, we can conclude that the observed nanoparticles are essentially identical

and localized near the film/electrolyte interface during the initial reduction of the film surface from NiO to Ni at high potentials.

To confirm this finding, several characterization methods were used to evaluate the initial lithiation of the thicker Ni/NiO electrodes. After the first discharge from the open circuit condition of the as-deposited film to 1.7 V, the samples were removed from the electrochemical cell and rinsed with dimethyl carbonate. The samples were then transferred from the glove box to the characterization chamber for XPS, ToF-SIMS depth profiling and STEM/EELS measurements. The samples were exposed briefly to ambient during this transfer.

Composition and chemical changes in the Ni/NiO films and its SEI were investigated using depth resolved XPS. Fig. 5 shows sputter depth profiles of Ni and Li species on the Ni (34 Å) / NiO (65 Å) bilayer electrode. As seen in Fig. 5A, signal from Ni is observed in the SEI layer far above the

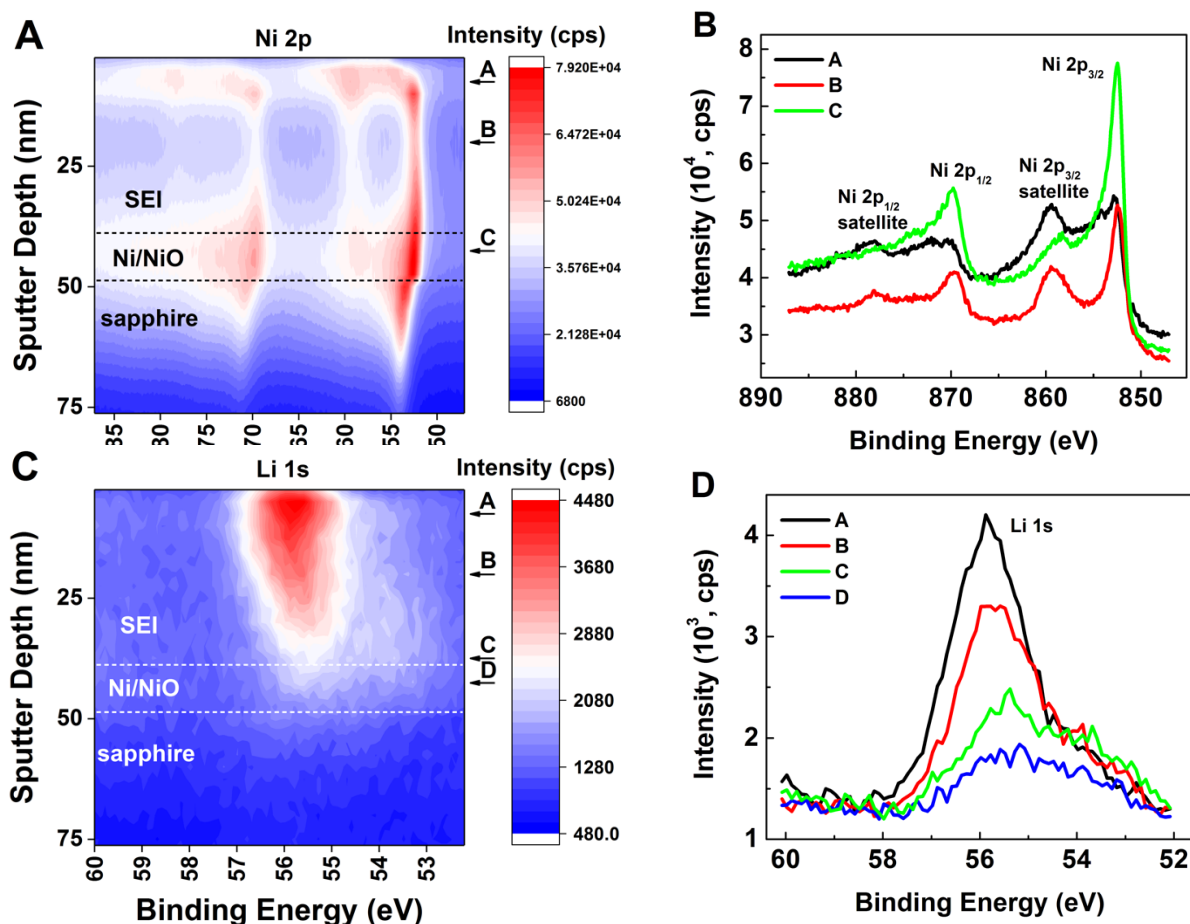


Fig. 5 XPS depth profiles of (A) Ni 2p and (C) Li 1s peaks for the Ni (34 Å) / NiO (65 Å) bilayer electrode after the first discharge from 3.3 V (the open circuit potential of the as-deposited electrode) to 1.7 V. (B) and (D) show Ni 2p and Li 1s spectra at depth positions marked by arrows in A and C, correspondingly.

electrode surface with a distinctive shift to higher binding energy when the sputter beam goes through the film. Previous research has supported the assignment of the Ni 2p_{3/2} XPS spectra with binding energies of 852.9 eV to Ni⁰ and 854.5 eV to Ni²⁺ in nickel oxides.^{48,49} Fig. 5 shows the Ni 2p_{3/2} peak at 852.7 eV that indicates a presence of nickel metal in the SEI layer. There is some spreading of intensity to the higher binding energy of 855 eV as the sputter beam approaches the NiO layer. Since the spatial resolution of XPS depth profiling is about 10 nm, it is hard to distinguish between signal from the individual Ni and NiO layers in the experimental spectrum. In addition, Ni oxide (as many other oxides) is very sensitive to ion beam damage and sputtering can lead to some reduction of NiO to Ni.⁵⁰ For the same reasons, we cannot determine a localization of Li inside the Ni/NiO film, but XPS data show definite shifting of the Li 1s peak to lower binding energies. A single Li 1s peak at 55.8 eV is observed reasonably far from the film surface. Combined with the observed fluorine signal at 685.1 eV (Fig. S5), this suggests that LiF is a major component of the SEI.⁵¹ As the sputter beam approaches and finally penetrates the film, intensity of this peak decreases and a mixed phase of Li⁺ (55.5 eV) and Li metal (53.8 eV) is observed.⁵² Despite the shortcomings of XPS mentioned above, XPS analysis shows that reduced Ni is found outside of the Ni/NiO bilayer film and confirms our XRR/GISAXS findings about initial lithiation of the surface NiO layer at theoretically predicted potential.

The presence of nickel in the SEI layer covering the Ni/NiO film after discharge from 3.3 V (i.e., the open circuit potential of the as-deposited film) to 1.7 V was confirmed with ToF-SIMS depth profiling of the same sample (Fig. S6). ToF-SIMS depth profiling was done using the same conditions for the test sample of Ni/NiO/PMMA as a reference to eliminate resolution effect. Fig. S7A shows ToF-SIMS profiles for this Ni/NiO/PMMA film. Fig. S7B compares the Ni depth profiles of the pristine Ni/NiO film coated by PMMA and the initially lithiated film with a thick SEI layer. It is obvious from this comparison that some reduced Ni migrates to the NiO-electrolyte interface and that nanoparticles of Ni were “frozen” in the formed SEI layer. It should be noted that only a qualitative estimation of elements can be done from the data because of different sensitivity factors of SIMS for different elements and different matrices.⁵³

Cross-section samples of the bilayer films were studied via TEM, STEM, and EELS to further corroborate the X-ray reflectivity studies. Fig. 6A shows the overall morphology of the bilayer film after electrochemical first cycle discharging of the sample from the open circuit potential for the as-deposited sample (3.3 V) to a potential of 1.7 V. The Ni and NiO layers were measured to be approximately 50 Å and 80 Å thick, respectively, with SEI formation on top of the film. A rough layer, less than 10 Å thick, was observed at the interface between the NiO layer and the SEI. This layer is marked by a white arrow

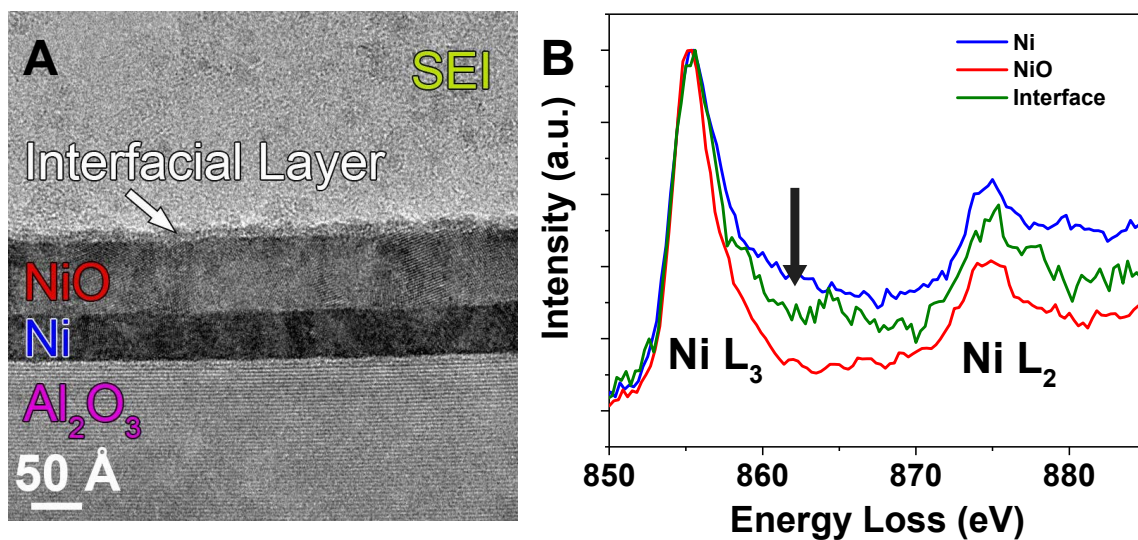


Fig. 6 TEM and EELS analysis of the bilayer Ni/NiO film after electrochemical first cycle discharging of the sample from the open circuit potential for the as-deposited sample to potential of to 1.7 V. (A) TEM image of cross-section morphology, showing the <10 Å interfacial layer that formed. (B) Core-loss EELS spectra of the Ni L_3 and L_2 edges collected from the Ni (blue), NiO (red), and interfacial layers (green) in the cross-section.

in Fig. 6A. Interestingly, the position of this interfacial layer corresponds with the region of lower electron density that was observed via X-Ray reflectivity in Fig. 1B. EELS characterization was carried out to confirm the composition and chemical state of the bilayer film structure after lithiation. Fig. 6B shows the Ni L_3 and L_2 edges, which can be used to determine the Ni oxidation state, as the edges represent the $O\ 2p \rightarrow Ni\ 3d$ electron transition and directly probe the Ni $3d$ orbital occupancy.⁵⁴ The intensity ratio of the L_3/L_2 edges increase as the oxidation state of Ni increases.⁵⁴ Calculation of this intensity ratio gives the NiO (Ni^{2+}) layer a L_3/L_2 ratio of 1.58 whereas the Ni (Ni^0) layer has a L_3/L_2 ratio of 1.35. The calculated L_3/L_2 value of the interfacial layer was 1.49, suggesting it has a lower oxidation state than Ni^{2+} . We also observe that the Ni L_3 edge of the interfacial layer has a more intense tail feature (860 eV – 870 eV) which is strongly characteristic of Ni^0 .⁵⁵ Overall, TEM images together with EELS characterization suggest that the rough interfacial layer is Ni^0 rich compared to the NiO layer underneath it. Falling electron densities in the same region revealed by X-ray reflectivity would suggest the initial formation Ni and Li_2O reaction products that together have a lower electron density than NiO. As such, the two characterization methods suggest that the observed changes in morphology and composition are associated with the initial processes of NiO conversion.

The presence of Li in the structure was also confirmed by observing the Li K edge signature in the low-loss EELS region at ~ 60 eV. This is seen in Fig. 7, which highlights a portion of an EELS linescan

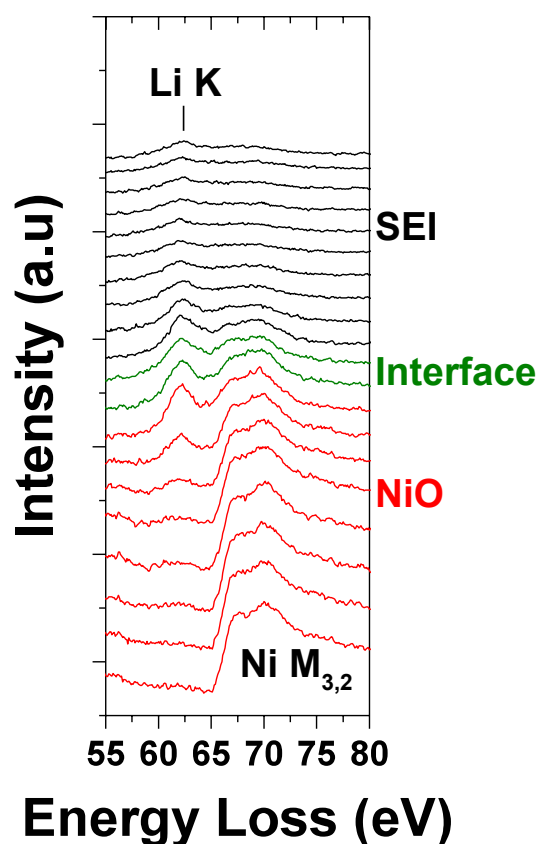


Fig. 7 EELS linescan of the SEI/NiO interfacial region. Spectra collected from the SEI are shown in black, whereas spectra from the interfacial layer and NiO are shown in green and red, respectively.

collected in the region of the SEI, interfacial layer, and top half of the NiO layer seen in Figure 6A. The entire linescan analysis region is shown in Fig. S8.

This linescan used a step-size of 5 Å in order to have high enough spatial resolution to capture the very thin interfacial layer. However, a 7 Å STEM probe size was needed in order to have strong enough EELS signal. Consequently, there is some spatial oversampling in the linescan, and the data collected from the interfacial layer likely includes partial contribution from the surrounding regions. Nevertheless, Fig. 7 shows the presence of Li in the SEI, interfacial layer, and the very top region of the NiO layer. Integrating the linescan regions from each individual layer, as shown in Fig. S8B, also helps reveal the Li distribution for the whole structure. The fine structure of the Li K edge in the SEI suggests the presence of LiF, as was seen via XPS.⁵⁶ This EELS data reinforces the *operando* X-ray measurement findings that in addition to the formation of an interfacial layer at 1.7 V, there is some diffusion of Li into the NiO layer before significant conversion occurs.

Conclusions

Operando XRR and GISAXS measurements, *ex situ* XPS and ToF-SIMS depth profiling and TEM imaging with EELS analysis were used to probe the nucleation process and the reduced Ni morphology during initial lithiation near the theoretical lithiation potential of NiO thin film electrodes (1.8–2.0 V). Our studies reveal that conversion reactions and structural changes in NiO thin film electrodes begin at potentials of 1.8–2.2 V, near the theoretical lithiation potential. This initial stage of lithiation is characterized by (i) the diffusion of lithium ions into the electrode and the formation of low electron density region close to the buffer Ni layer; (ii) the roughening of the NiO film surface and (iii) the formation of reduced Ni in the form of $R_g \sim 16\text{--}20 \text{ \AA}$ nanoparticles within the SEI.

These data suggest a dissolution process of the surface of the NiO electrode precedes the conversion reaction. This process could be impacted by lithium adsorption and incorporation at the buried interface or could simply be the byproduct of radical ions formed by trace water or reduction of the electrolyte during the first discharge. Evidence of the dissolution can be seen by the pronounced roughening of the film surface by XRR and the substantial nickel signal in the SEI found by XPS, SIMS, and TEM for electrodes after first cycle discharging of the sample from the open circuit potential for the as-deposited sample to potential of 1.7 V. These dissolved Ni^{2+} ions would electrochemically reduce at 2.7 V w.r.t. Li/Li^+ or lower, in agreement with the Ni^0 species found by XPS. This process is intrinsically similar to the shuttling of dissolved transition metal cations from lithium metal oxide cathodes to anode surface.⁵⁷⁻⁶² The reduction of these metal ions is known to accelerate the formation of the SEI,⁶¹⁻⁶⁵ suggesting that the surface particles measured by GISAXS above 2 V could very well be the nucleation of Ni-catalyzed SEI products. Taken together, these studies provide a new window into processes occurring though the metal oxide electrodes before bulk conversion reactions take place, at both the buried metal/oxide interface and the surface of the oxide itself.

Conflicts of interest

There are no conflicts to declare.

Acknowledgments

This research was supported by the Center for Electrochemical Energy Science, an Energy Frontier Research Center funded by the U.S. Department of Energy, Office of Science, Office of Basic Energy Sciences, under Contract No. DE-AC02-06CH11357. We thank the beamline staff at 33BM and 12ID, Advanced Photon Source (APS), which provided valuable assistance. The samples were grown in the

Northwestern University Materials Research Center Pulsed Laser Deposition Facility supported by the National Science Foundation MRSEC program (DMR-1720139). The electron microscopy and XPS/ToF-SIMS work made use of the EPIC and Keck-II facilities of Northwestern University's NUANCE Center, which is supported by the Soft and Hybrid Nanotechnology Experimental (SHyNE) Resource (NSF ECCS-1542205); the MRSEC program (NSF DMR-1720139) at the Materials Research Center; the International Institute for Nanotechnology (IIN); the Keck Foundation; and the State of Illinois, through the IIN. We also acknowledge the use of the X-ray Diffraction Facility also supported by MRSEC and SHyNE.

References

1. K. Xu, Nonaqueous liquid electrolytes for lithium-based rechargeable batteries, *Chem. Rev.*, 2004, **104**(10), 4303–4418.
2. H. Li, H. Zhou, Enhancing the performances of Li-ion batteries by carbon-coating: present and future, *Chem. Commun.*, 2012, **48**(9), 1201-1217.
3. K. Xu, Electrolytes and interphases in Li-ion batteries and beyond, *Chem. Rev.*, 2014, **114**(23), 11503-11618.
4. M. Gauthier, T. J. Carney, A. Grimaud, L. Giordano, N. Pour, H.-H. Chang, D. P. Fenning, S. F. Lux, O. Paschos, C. Bauer, F. Maglia, S. Lupart, P. Lamp, Y. Shao-Horn, Electrode-electrolyte interface in Li-ion batteries: current understanding and new insights, *J. Phys. Chem. Lett.*, 2015, **6**(22), 4653-4672.
5. T. Minato, T. Abe, Surface and interface sciences of Li-ion batteries - research progress in electrode-electrolyte interface, *Prog. Surf. Sci.*, 2017, **92**(4), 240-280.
6. P. Poizot, P.; Laruelle, S.; Grugeon, S.; Dupont, L.; Tarascon, J. M. Nano-Sized Transition-Metaloxides as Negative-Electrode Materials for Lithium-Ion Batteries. *Nature* **2000**, *407* (6803), 496-499.
7. V. Etacheri, R. Marom, R. Elazari, G. Salitra, D. Aurbach, Challenges in the development of advanced Li-ion batteries: a review, *Energy Environ. Sci.*, 2011, **4**(9), 3243–3262.
8. M. S. Whittingham, Ultimate limits to intercalation reactions for lithium batteries, *Chem. Rev.*, 2014, **114**(23), 11414–11443.
9. A. Kraytsberg, Y. A. Ein-Eli, Critical review-promises and barriers of conversion electrodes for Li-ion batteries, *J. Solid State Electrochem.*, 2017, **21**(7), 1907-1923.
10. J. Cabana, L. Monconduit, D. Larcher, M. R. Palacín, Beyond intercalation-based Li-ion batteries: the state of the art and challenges of electrode materials reacting through conversion reactions, *Adv. Mater.*, 2010, **22**(35), E170-E192.
11. N. Nitta, G. Yushin, High-capacity anode materials for lithium-ion batteries: choice of elements and structures for active particles, *Part. Part. Syst. Character.*, 2014, **31**(3), 317-336.
12. R. W. Balluffi, S. M. Allen, W. C. Carter, *Kinetics of Materials*, Wiley-Interscience, Hoboken, New Jersey, 2005.
13. H. Li, P. Balaya, J. Maier, Li-storage via heterogeneous reaction in selected binary metal fluorides and oxides, *J. Electrochem. Soc.*, 2004, **151**(11), A1878-A1885.
14. C.-X. Zu, H. Li, Thermodynamic analysis on energy densities of batteries, *Energy Environ. Sci.*, 2011, **4**(8), 2614-2624.

15. J. Ho, M. L. Coote, C. J. Cramer, D. G. Truhlar, Theoretical calculation of reduction potentials. In *Organic Electrochemistry*, Hammerich, O., Speiser, B., Eds.; CRC Press, Boca Raton, FL, 5th ed., 2015, pp. 229-259.
16. Z. P. Yao, S. Kim, M. Aykol, Q. Q. Li, J. S. Wu, J. G. He, C. Wolverton, Revealing the conversion mechanism of transition metal oxide electrodes during lithiation from first-principles, *Chem. Mater.*, 2017, **29** (21), 9011-9022.
17. G. Evmenenko, R. Warburton, H. Yildirim, J. Greeley, M. Chan, B. Buchholz, P. Fenter, M. Bedzyk, T. Fister, Understanding the role of overpotentials in lithium ion conversion reactions: visualizing the interface, *ACS Nano* (2018), *submitted*.
18. S. Grugeon, S. Laruelle, R. Herrera-Urbina, L. Dupont, P. Poizot, J. M. Tarascon, Particle size effects on the electrochemical performance of copper oxides toward lithium, *J. Electrochem. Soc.*, 2001, **148**(4), A285–A292.
19. H. Liu, G. Wang, J. Liu, S. Qiao, H. Ahn, Highly ordered mesoporous NiO anode material for lithium ion batteries with an excellent electrochemical performance, *J. Mater. Chem.*, 2011, **21**(9), 3046–3052.
20. J. Ma, J. Yang, L. Jiao, Y. Mao, T. Wang, X. Duan, J. Lian, W. Zheng, NiO nanomaterials: controlled fabrication, formation mechanism and the application in lithium-ion battery, *Cryst. Eng. Commun.*, 2012, **14**(2), 453–459.
21. X. Wang, L. Qiao, X. Sun, X. Li, D. Hu, Q. Zhang, D. He, Mesoporous NiO nanosheet networks as high performance anodes for Li ion batteries, *J. Mater. Chem. A*, 2013, **1**(13), 4173–4176.
22. M. V. Reddy, G. V. S. Rao, B. V. R. Chowdari, Metal oxides and oxysalts as anode materials for Li ion batteries, *Chem. Rev.*, 2013, **113**(7), 5364-5457.
23. X. Wang, X. Li, X. Sun, F. Li, Q. Liu, Q. Wang, D. He, Nanostructured NiO electrode for high rate Li-ion batteries, *J. Mater. Chem.*, 2011, **21**(11), 3571–3573.
24. X. Wang, Z. Yang, X. Sun, X. Li, D. Wang, P. Wang, D. He, NiO nanocone array electrode with high capacity and rate capability for Li-ion batteries, *J. Mater. Chem.*, 2011, **21**(27), 9988–9990.
25. Z. Bai, Z. Ju, C. Guo, Y. Qian, B. Tang, S. Xiong, Direct large-scale synthesis of 3D hierarchical mesoporous NiO microspheres as high-performance anode materials for lithium ion batteries, *Nanoscale*, 2014, **6**(6), 3268-3273.
26. X. Sun, W. Si, X. Liu, J. Deng, L. Xi, L. Liu, C. Yan, O. G. Schmidt, Multifunctional Ni/NiO hybrid nanomembranes as anode materials for high-rate Li-ion batteries, *Nano Energy*, 2014, **9**, 168-175.
27. W. Sun, X. Rui, J. Zhu, L. Yu, Y. Zhang, Z. Xu, S. Madhavi, Q. Yan, Ultrathin nickel oxide nanosheets for enhanced sodium and lithium storage, *J. Power Sources*, 2015, **274**, 755-761.
28. C. Wang, Y. Zhao, D. Su, C. Ding, L. Wang, D. Yan, J. Li, H. Jin, Synthesis of NiO nano octahedron aggregates as high-performance anode materials for lithium ion batteries, *Electrochim. Acta*, 2017, **231**, 272-278.
29. J. Jan Kaspar, M. S. Bazarjani, C. Schitco, A. Gurlo, M. Graczyk-Zajac, R. Riedel, Electrochemical study of NiO nanosheets: toward the understanding of capacity fading, *J. Mater. Sci.*, 2017, **52**(11), 6498-6505.
30. C. Y. Ding, L. J. Wang, W. W. Zhou, D. Wang, Y. Du, G. W. Wen, New design on Li-ion battery anode of ternary complex metal/metal oxide@CNT: A case study of hierarchical NiCo-NiCo₂O₄@CNTs, *Chem. Eng. Sci.* 2018, 353, 340-349.
31. E. Edison, A. Chaturvedi, H. Ren, S. Sreejith, C. T. Lim, S. Madhavi, Route of irreversible transformation in layered tin thiophosphite and enhanced lithium storage performance, *ACS Appl. Energy Mater.* 2018, **1**(10), 5772-5778.
32. X. L. Chen, T. Xiao, S. L. Wang, J. Li, P. Xiang, L. H. Jiang, X. Y. Tan, Superior Li-ion storage performance of graphene decorated NiO nanowalls on Ni as anode for lithium ion batteries, *Mater. Chem. Phys.* 2019, **222**, 31-36.

33. Y. M. Huang, J. X. Ouyang, X. Tang, Y. Yang, J. F. Qian, J. T. Lu, L. Xiao, L. Zhuang, NiGa₂O₄/rGO composite as long-cycle-life anode material for lithium-ion batteries, *ACS Appl. Mater. Interfaces* 2019, **11**(8), 8025-8031.
34. G. Evmenenko, T. T. Fister, D. B. Buchholz, Q. Li, K.-S. Chen, J. Wu, V. P. Drawid, M. C. Hersam, P. Fenter, M. J. Bedzyk, Morphological evolution of multilayer Ni/NiO thin film electrodes during lithiation, *ACS Appl. Mater. Interfaces*, 2016, **8**(31), 19979-19986.
35. G. Evmenenko, T. T. Fister, D. B. Buchholz, F. C. Castro, Q. Li, J. Wu, V. P. Drawid, P. Fenter, M. J. Bedzyk, Lithiation of multilayer Ni/NiO electrodes: criticality of nickel layer thicknesses on conversion reaction kinetics, *Phys. Chem. Chem. Phys.*, 2017, **19**(30), 20029-20039.
36. M. D. Irwin, D. B. Buchholz, A. W. Hains, R. P.H. Chang, T. J. Marks, p-Type semiconducting nickel oxide as an efficiency-enhancing anode interfacial layer in polymer bulk-heterojunction solar cells, *Proc. Natl. Acad. Sci. U.S.A.*, 2008, **105**(8), 2783-2787.
37. M. D. Irwin, J. D. Servaites, D. B. Buchholz, B. J. Leever, J. Liu, J. D. Emery, M. Zhang, J.-H. Song, M. F. Durstock, A. J. Freeman, M. J. Bedzyk, M. C. Hersam, R. P. H. Chang, M. A. Ratner, T. J. Marks, Structural and electrical functionality of NiO interfacial films in bulk heterojunction organic solar cells, *Chem. Mater.*, 2011, **23**(8), 2218-2226.
38. E. Karapetrova, G. Ice, J. Tischler, H. W. Hong, P. Zschack, Design and performance of the 33-BM beamline at the Advanced Photon Source, *Nucl. Instrum. Methods. Phys. Res. Sect. A*, 2011, **649**(1), 52-54.
39. T. T. Fister, B. R. Long, A. A. Gewirth, B. Shi, L. Assoufid, S. S. Lee, P. Fenter, Real-time observations of interfacial lithiation in a metal silicide thin film, *J. Phys. Chem. C*, 2012, **116**(42), 22341-22345.
40. A. Nelson, Co-refinement of multiple-contrast neutron/X-ray reflectivity data using MOTOFIT, *J. Appl. Crystallogr.*, 2006, **39**(2), 273-276.
41. B. Lee, GISAXSshop: GISAXS data reduction program. <https://sites.google.com/site/byeongdu/software> 2014.
42. J. Ilavsky, P. R. Jemian, Irena: tool suite for modeling and analysis of small-angle scattering, *J. Appl. Crystallogr.*, 2009, **42**(2), 347-353.
43. M. W. Roberts, R. S. Smart, The defect structure of nickel oxide surfaces as revealed by photoelectron spectroscopy, *J. Chem. Soc., Faraday Trans. 1*, 1984, **80**(11), 2957-2968.
44. A. Hexemer, P. Müller-Buschbaum, Advanced grazing-incidence techniques for modern soft-matter material analysis, *IUCrJ* 2015, **2**, 106-125.
45. Y. Yoneda, Anomalous surface reflection of X-rays, *Phys. Rev.*, 1963, **131**(5), 2010-2013.
46. A. Senesi, B. Lee, Scattering functions of polyhedral, *J. Appl. Crystallogr.*, 2015, **48**(2), 565-577.
47. A. Guinier, G. Fournet, *Small-angle scattering of X-rays*, Wiley, New York, 1955.
48. S. Oswald, W. Brückner, XPS depth profile analyses of non-stoichiometric NiO films, *Surf. Interface Anal.*, 2004, **36**(1), 17-22.
49. A. P. Grosvenor, M. C. Biesinger, R. St. C. Smart, N. S. McIntyre, New interpretation of XPS spectra of nickel and oxides, *Surf. Sci.*, 2006, **600**(9), 1771-1779.
50. D. F. Mitchell, G. I. Sproule, M. J. Graham, Sputter reduction of oxides by ion bombardment during auger depth profile analysis, *Surf. Interface Anal.*, 1990, **15**(8), 487-497.
51. K. W. Schroder, H. Celio, L. J. Webb, K. J. Stevenson, Examining solid electrolyte interphase formation on crystalline silicon electrodes: influence of electrochemical preparation and ambient exposure conditions, *J. Phys. Chem. C*, 2012, **116**(37), 19737-19747.
52. S. Tanaka, M. Taniguchi, H. Tanigawa, XPS and UPS studies on electronic structure of Li₂O, *J. Nucl. Mater.*, 2000, **283-287**, 1405-1408.
53. D. Alamarguy, J. E. Castle, M. Liberatore, F. Decker, Distribution of intercalated lithium in V₂O₅ thin films determined by SIMS depth profiling, *Surf. Interface Anal.*, 2006, **38**(4), 847-850.

54. J. Graetz, C. C. Ahn, H. Ouyang, P. Rez, B. Fultz, White lines and D-band occupancy for the 3d transition-metal oxides and lithium transition-metal oxides, *Phys. Rev. B - Condens. Matter Mater. Phys.*, 2004, **69**(23), 1-6.
55. E. C. Dickey, V. P. Dravid, P. D. Nellist, D. J. Wallis, S. J. Pennycook, A. Revcolevschi, Structure and bonding at Ni-ZrO₂ (cubic) interfaces formed by the reduction of a NiO-ZrO₂ (cubic) composite, *Microsc. and Microanal.*, 1997, **3**(5), 443-450.
56. F. Wang, J. Graetz, M. S. Moreno, C. Ma, L. Wu, V. Volkov, Y. Zhu, Chemical distribution and bonding of lithium in intercalated graphite: identification with optimized electron energy loss spectroscopy, *ACS Nano*, 2011, **5**(2), 1190–1197.
57. L. Yang, M. Takahashi, B. Wang, A study on capacity fading of lithium-ion battery with manganese spinel positive electrode during cycling, *Electrochim. Acta*, 2006, **51**(16), 3228-3234.
58. I. H. Cho, S.-S. Kim, S. C. Shin, N.-S. Choi, Effect of SEI on capacity losses of spinel lithium manganese oxide/graphite batteries stored at 60°C, *Electrochem. Solid-State Lett.*, 2010, **13**(11), A168-A172.
59. C. Zhan, J. Lu, A. J. Kropf, T. Wu, A. N. Jansen, Y.-K. Sun, X. Qiu, K. Amine, Mn(II) deposition on anodes and its effects on capacity fade in spinel lithium manganate–carbon systems, *Nat. Commun.*, 2013, **4**, 2437.
60. S. Gowda, K. G. Gallagher, J. Croy, M. Bettge, M. M. Thackeray, M. Balasubramanian, Oxidation state of cross-over manganese species on the graphite electrode of lithium-ion cells, *Phys. Chem. Chem. Phys.*, 2014, **16**(15) 6898-6902.
61. J. A. Gilbert, I. A. Shkrob, D. P. Abraham, Transition metal dissolution, ion migration, electrocatalytic reduction and capacity loss in lithium-ion full cells, *J. Electrochem. Soc.*, 2017, **164**(2), A389-A399.
62. C. Zhan, T. Wu, J. Lu, K. Amine, Dissolution, migration, and deposition of transition metal ions in Li-ion batteries exemplified by Mn-based cathodes – a critical review, *Energy Environ. Sci.*, 2018, **11**(2), 243-257.
63. C. Delacourt, A. Kwong, X. Liu, R. Qiao, W. L. Yang, P. Lu, S. J. Harris, V. Srinivasan, Effect of manganese contamination on the solid-electrolyte-interphase properties in Li-ion batteries, *J. Electrochem. Soc.*, 2013, **160**(8), A1099-A1107.
64. T. Joshi, K. Eom, G. Yushin, T. F. Fuller, Effects of dissolved transition metals on the electrochemical performance and SEI growth in lithium-ion batteries, *J. Electrochem. Soc.*, 2014, **161**(12), A1915-A1921.
65. O. C. Harris, M. H. Tang, Molecular probes reveal chemical selectivity of the solid-electrolyte interphase, *J. Phys. Chem. C*, 2018, **122**(36) 20632-20641.